

# Variations in crustal structure across the transition from West to East Antarctica, Southern Victoria Land

S. Bannister,<sup>1</sup> J. Yu,<sup>1</sup> B. Leitner<sup>2\*</sup> and B. L. N. Kennett<sup>3</sup>

<sup>1</sup>*Institute of Geological and Nuclear Sciences, PO Box 30368, Lower Hutt 6315, New Zealand*

<sup>2</sup>*Institute of Geological and Nuclear Sciences, Dunedin, New Zealand*

<sup>3</sup>*Research School of Earth Sciences, Australian National University, Canberra, ACT 0200, Australia*

Accepted 2003 July 1. Received 2003 May 23; in original form 2002 August 12

## SUMMARY

The crustal structure beneath Ross Island and the Transantarctic Mountains (TAM) in Southern Victoria Land, Antarctica, is inferred using non-linear inversion of receiver functions, derived from teleseismic earthquake data. Intermediate-period waveforms from more than 160 teleseismic earthquakes recorded between January 1994 and January 2000 were used in the analysis. The inversion results confirm a crustal thickness of 19–21 km beneath Ross Island, consistent with previous multichannel seismic work. In addition we observe a crustal thickness of 18–20 km beneath the Ross Sea coastline immediately adjacent to the TAM. Further inland, beneath the TAM, the estimated Moho depths range from 30–33 km (~30 km from the coast) to 36–40 km (~85 km from the coast), deepening away from the coast beneath the TAM. These results are in broad agreement with previous seismic and gravity interpretations. Beneath the TAM a sharp mid-crustal discontinuity is present at 8–14 km depth beneath the eastern-most stations, but absent on the western side of the TAM, indicating a spatial change in the mid-crustal composition.

**Key words:** Antarctica, crustal structure, inversion, Moho discontinuity, seismic velocity, shear wave, waveform analysis.

## 1 INTRODUCTION

The Transantarctic Mountains (TAM, Fig. 1a) form the morphological and geological boundary between East and West Antarctica, reaching elevations of over 4500 m and spanning in length over 3500 km. The TAM are inferred to have undergone up to 6 km of uplift during the Cenozoic, starting around ~55 Ma (Fitzgerald 1992), although some exhumation also occurred in the Cretaceous (Fitzgerald 1995), with uplift and denudation of the TAM complete before ~15 Ma. (Sugden *et al.* 1999).

To the east of the TAM lies the West Antarctic Rift System (WARS, Fig. 1a), a broad region of stretched continental or underplated oceanic crust which is mostly either subglacial or submerged. The crust in the WARS is inferred to have undergone extension mainly in the Cretaceous, but with some Cenozoic episodes (Behrendt *et al.* 1991a,b), and varies in thickness between 17 and 21 km (e.g. Trehu *et al.* 1989; Trey *et al.* 1997; Cooper *et al.* 1997). Within the West Antarctic Rift System, and immediately adjacent to the TAM lies the Victoria Land sedimentary basin (VLB, Fig. 1b), which has a sedimentary thickness of ~14 km, including at least 4–5 km of Cenozoic sediments (McGinnis *et al.* 1985; Cooper *et al.* 1987). There is some evidence from seismic data of crustal thin-

ning beneath the eastern flank of the VLB (Cooper *et al.* 1997), and high heat flows are observed in the region (e.g. 83–126 m Wm<sup>-2</sup>, Blackman *et al.* 1987; Della Vedova *et al.* 1992; Berg *et al.* 1989). Recent (Neogene and younger) faulting (Cooper *et al.* 1987) as well as magmatic activity (Behrendt *et al.* 1991b) has occurred in the Terror Rift (Fig. 1b), inside the VLB. Present-day alkaline volcanism is represented by Mt Erebus (Fig. 1b) in the Ross volcanic Archipelago (LeMasurier 1990) at the southern end of the Terror Rift, as well as by Mt Melbourne (Fig. 1b), at the northern end.

The uplift mechanism for the Transantarctic mountains remains unresolved, with continuing debate over the nature of the interaction between the uplift of the TAM and the rift extension episodes in the VLB and West Antarctic rift system. Proposed mechanisms for the TAM uplift include isostatic rebound due to stretching of the lithosphere (e.g. Bott & Stern 1992), thermal uplift due to heat conduction or advection from extended upper mantle (Stern & ten Brink 1989), and rebound after erosion (e.g. Stern & ten Brink 1989), amongst others.

Some of these mechanisms require certain assumptions about the crustal and upper-mantle structure beneath the eastern side of the TAM, the 'TAM Front', as well as about the timing of the rift-related processes in the nearby VLB. However there is only limited information on the physical properties of the crust beneath the TAM, and on the nature of the crustal transition between the VLB and the TAM. Fundamental information is still required about the crustal

\*Now at: Geosphere Ltd, PO Box 44285, Lower Hutt, New Zealand.

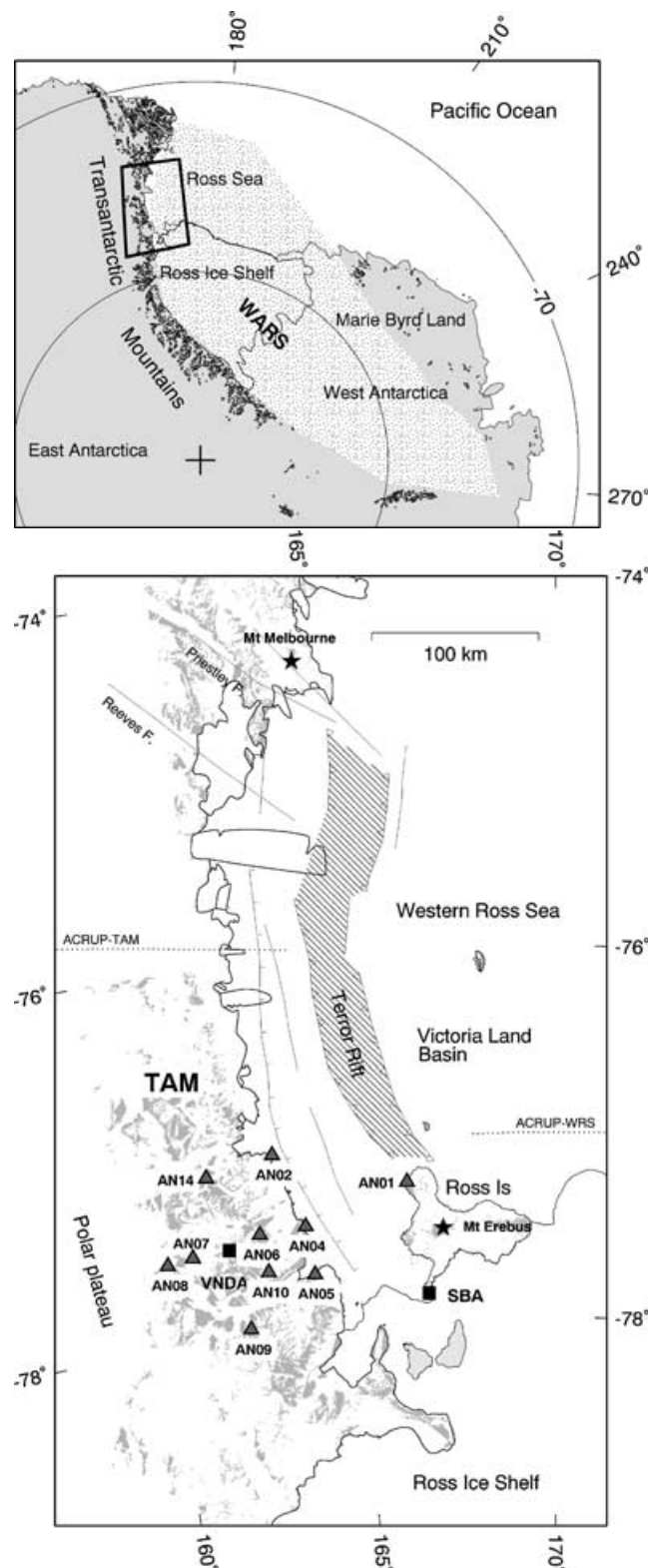


**Figure 1.** (a) The Ross Sea region, showing the location of the study region (outlined rectangle), the West Antarctic Rift System (WARS) (shaded in light stipple), and the Transantarctic Mountains. (b) The western Ross Sea region, Antarctica, showing the location of active volcanoes (stars), the Victoria Land Basin, the Terror Rift, and the Transantarctic Mountains (TAM), with exposed onshore rock outcrops shaded light grey. ACRUP seismic lines (Cooper *et al.* 1997) are shown as dotted lines. Permanent seismograph stations VNDA and SBA are marked as solid-filled squares, and the locations of temporary broad-band seismometers are shown as filled triangles.

thickness, velocity and thermal structure, and the nature of the major lithospheric and crustal boundaries in the region. Some constraints have already been provided by gravity studies (e.g. Reitmayr 1997; Davey & Cooper 1987), and by seismic reflection data (O'Connell & Stepp 1993; Della Vedova *et al.* 1997). Data from the latter (ACRUP) seismic study indicate thickening crust beneath the TAM to a depth of 38 km, and quite low  $P$ -wave velocities ( $7.6\text{--}7.7\text{ km s}^{-1}$ ) in the mantle beneath the VLB (Della Vedova *et al.* 1997) while slow  $S$ -wave velocities are inferred at 60–160 km depth from surface wave analysis (Bannister *et al.* 1999a), suggesting that the upper-mantle is anomalously warm at that depth.

This paper focuses on a study of the crustal structure of the TAM using broad-band seismic recordings of earthquakes. We provide new constraints on the  $S$ -wave velocity structure of the TAM and Ross Island region, by examining receiver functions derived from teleseismic waveform data. The data were primarily derived from a broad-band seismometer array, which was deployed in the Transantarctic Mountains in Southern Victoria Land during 1999–2000. We also use data recorded between 1994 and 2000 by two permanent stations.

## 2 DATA AND METHODOLOGY

This study concentrates on examining crustal structure beneath the Transantarctic Mountains using observations of  $P$ -to- $S$  ( $P_s$ ) conversions generated at the Moho, and at other interfaces within the crust, by teleseismic earthquake waves.  $P_s$  converted energy can be estimated using the broad-band teleseismic receiver function method (RF) (e.g. Langston 1977; Owens & Zandt 1985; Ammon *et al.* 1990; Ammon 1991), which aims to eliminate source-related and mantle-path effects, leaving only reverberations associated with crustal and mantle structure near the receiver, the 'receiver function' (RF). Derived RFs primarily consist of  $P_s$  phases associated with seismic discontinuities, such as the Moho, beneath the stations (e.g. Owens & Zandt 1985). The differential times, amplitudes and polarities of the phases contain information about the nature of the discontinuities. A useful numerical investigation of receiver functions is given by Cassidy (1992).

Receiver function analysis popularly involves deconvolving the vertical component seismogram from the radial and tangential component seismograms (e.g. Langston 1977; Ammon 1991). Here instead the receiver functions are derived using multiple-taper spectral correlation (Park & Levin 2000), a new method for multiple-record RF estimation which is a variant of the damped spectral division technique (Ammon 1991).

We primarily use waveform data recorded by a temporary broad-band array, which was deployed in the central TAM during the 1999–2000 austral summer (Fig. 1b). The purpose of the array was to record teleseismic data for this RF study, as well as to investigate regional seismicity. The seismometer array had an average station spacing of 20–25 km, and straddled the Transantarctic Mountains opposite Ross Island, with array stations located on the East Antarctic craton near the edge of the polar plateau (e.g. AN08, Fig. 1b), as well as over the Victoria Land Basin (e.g. station AN01, Fig. 1b). Each array station included either a Guralp 40T or 3ESP broad-band seismometer, with an accompanying Orion recorder.

Suitable teleseismic earthquakes (Fig. 2) were selected by searching the IRIS-DMC catalogues on the basis of epicentral distance ( $25^\circ < \Delta < 100^\circ$ ) and magnitude (greater than 5.5). This distance range was used to avoid problems with regional and core phases (e.g. events beyond  $103^\circ$  would involve emergent  $P_{\text{diff}}$  arrivals). About 80 such teleseismic events were recorded by the temporary array, 64 of which had a reasonable signal to noise ratio.

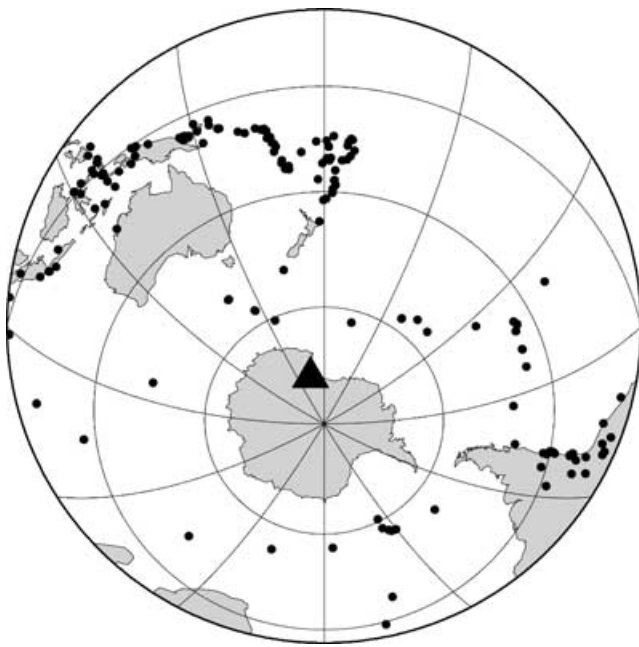


**Figure 2.** Distribution of all of the earthquakes that were used in the receiver function study. The location of the study region is marked by a large triangle.

Data recorded at two permanent seismograph stations VNDA and SBA were also used for this study. VNDA is a USGS-supported digital three component borehole seismometer situated in the Transantarctic Mountains, as part of the Global Telemetered Seismograph Network (GTSN) while SBA is effectively a backup station for VNDA, situated at Scott Base, Ross Island (Davey & Woodward 1995). The IRIS-DMC database for these two stations was searched for appropriate records on the basis of epicentral distance and magnitude, for the time period 1995–2000. Of the many teleseismic events, 94 (SBA) and 75 (VNDA) events recorded by the stations were chosen for further analysis.

Teleseismic receiver functions (RFs) were derived from the recorded data using multiple-taper spectral correlation (Park & Levin 2000). Only the first 50 s of the teleseismic *P*-wave coda was used for each individual RF. Individual frequency-domain RFs were bin-averaged in overlapping intervals of either epicentral distance or backazimuth, with  $5^\circ$  bins. Such averaging allows individual RFs to influence composite RFs in two adjacent bins (Park & Levin 2000). The term ‘backazimuth’ is used to refer to the direction from the station towards the earthquake epicentre, measured clockwise from north.

## 2.1 Non-linear inversion for velocity structure

Receiver functions are nonlinearly dependent on the shear wave velocity, and so velocity–depth profiles derived by linearized inversion of RFs can be strongly dependent on initial velocity models. Instead, in this study, velocity–depth profiles of the *S*-wave velocity structure beneath some of the stations were derived by applying the non-linear nearest-neighbourhood inversion technique of Sambridge (1999a,b). In this approach stochastic sampling is used to search multi-dimensional parameter space for the range of acceptable velocity models, using geometrical constructs known as Voronoi cells to assist in the search and appraisal stages (Sambridge 1999a). In our inversions the crustal structure was parametrized using 24 variables, 4 variables for each of 6 layers, describing the *S* ve-

locity at the top and bottom of the layer (allowing velocity gradients within the layer), the layer thickness, and the ratio of *P* to *S* velocity ( $V_p/V_s$ ) for that layer. Velocities were assumed to be isotropic, and the layers were assumed to be flat-lying. Details of the background behind the inversion technique, together with examples, are given by Sambridge (1998, 1999a,b).

## 3 RECEIVER FUNCTION OBSERVATIONS AND MODELLING

The main characteristics of the observed RFs are described below for the stations with good quality recordings. We examine variations in both the radial and transverse RFs. Significant energy on transverse RFs can be an indication of anisotropy (Savage 1998), dipping structure (e.g. Langston 1977; Peng & Humphreys 1997), or other complications such as near-receiver scattering. In general however there were low energy levels on the transverse data, and we focus on examining the radial RFs.

### 3.1 Central TAM, VNDA station

First we examine data from station VNDA (Fig. 1b), located at Bull Pass, in the central Transantarctic Mountains. The borehole is surrounded by extensive sills of Jurassic dolerite, which overlie plutonic basement and metamorphic rocks of Precambrian to Ordovician age (Turnbull *et al.* 1994). The data quality from VNDA station is some of the best in this study. Useful data were obtained from a good range of backazimuths. The radial and transverse RFs are shown in Fig. 3 for different backazimuths.

Strong similarities can be seen between the radial RFs for different backazimuths, with a clear positive pulse at  $4.3 \pm 0.3$  s observed

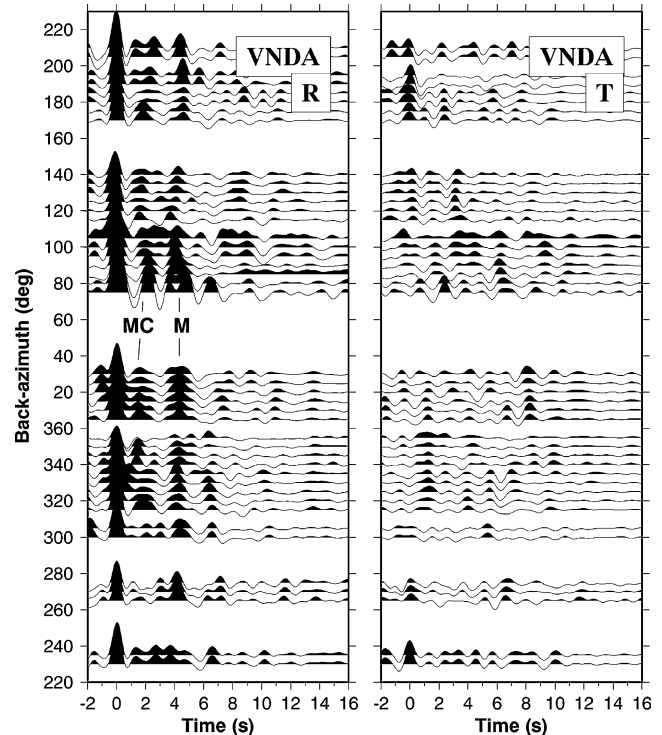


**Figure 3.** Radial (left) and transverse (right) receiver functions for station VNDA, plotted against backazimuth. A clear positive phase (marked as M) is observed at  $\sim 4.0$ – $4.5$  s which we interpret as a *Ps* conversion from Moho. Other earlier phases at 1–2 s time (marked as MC) represent conversions from mid-crustal discontinuities.

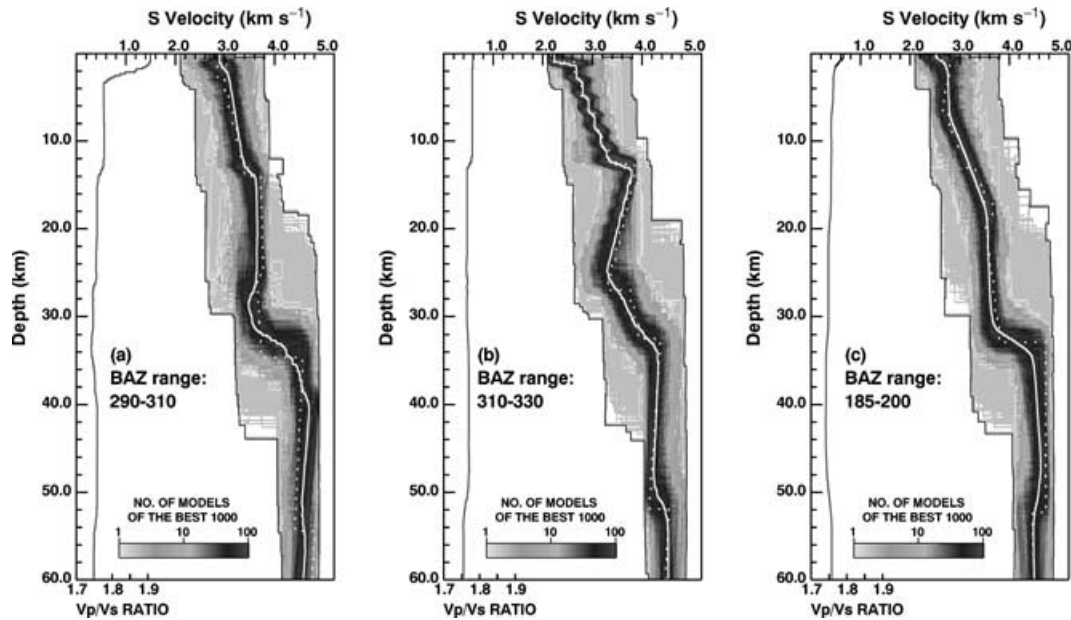


**Figure 4.** Seismic *S*-wave velocity models derived for station VNDA, resulting from non-linear inversion. All 5000 models searched in the inversion are shown by the outline of the light-grey-shading. The shaded regions indicate the density of the 1000 best models, the darkness being logarithmically proportional to the number of models, as shown by the scale bar. The solid white line represents the mean of the best 100 models, and the dotted white line represents the best of those models. The mean  $V_p/V_s$  ratio is shown on the left side of each of the models. Results are shown for backazimuths (a) 290°–310°. (b) 310°–330°. (c) 185°–200°.

behind the direct arrival. We interpret this phase as the converted *P<sub>s</sub>* phase resulting from the Moho discontinuity beneath the station. This *P<sub>s</sub>* phase has a relatively constant arrival time for most azimuths, although it appears to arrive slightly earlier, at ~4.0–4.1 s, for backazimuths between 80° and 120°. Such changes in the time of the radial *P<sub>s</sub>* with backazimuth may indicate the presence of dipping structure (e.g. Cassidy 1992; Levin & Park 1997). The earlier arrival time indicates either that waves arriving from the east are travelling downdip, or that the average crustal velocity is slightly faster to the east-southeast of the station.

A smaller positive pulse is also clear, at  $1.6 \pm 0.5$  s time. This pulse is quite coherent for most backazimuths, and has a relatively constant arrival time, although it is delayed about 0.3 s for event backazimuths of 76°–120°, and becomes complex between 330 and 360° backazimuth. We interpret this 1.6 s phase as a *P<sub>s</sub>* conversion resulting from a mid-crustal discontinuity.

The transverse RFs are also shown in Fig. 3. Some transverse energy is present at 0 s for backazimuths between 170° and 270°. The polarity of this pulse appears to change from negative to positive at a backazimuth between 80° and 100°, and again between 270° and 310° (Fig. 3). A later pulse is visible at ~1 to 1.5 s time, and is quite coherent at backazimuths between 315° and 30°. This pulse changes polarity between 35° and 90° backazimuth, and again between 300° and 315° (Fig. 3). It is probably related to the secondary pulse seen on the radial RFs at ~1.5 s; we note that the pulse time on the radial RFs changes rapidly between 315° and 30° backazimuth. Another pulse is observed at ~3 s time at backazimuths between 90° and 140°, slightly earlier in time than the *P<sub>s</sub>* phase seen on the radial RFs for the same backazimuth range.

These azimuthal changes in the energy on the transverse RFs likely represent the effect of tilted crustal discontinuities beneath the station placing *P*-wave energy on the transverse component (e.g. Langston 1977; Cassidy 1992; Owens *et al.* 1988). The transverse RFs between backazimuths 300°–100° are generally consistent with

a mid-crustal discontinuity with a dip direction to the east, although there is some inconsistency with this interpretation. At the least the changes in the transverse RFs suggest lateral changes in crustal structure beneath the station.

### 3.1.1 Inversion for *S*-wave velocity

We search for the range of *S*-wave velocity–depth models that satisfy the observed data using the non-linear nearest-neighbourhood inversion technique of Sambridge (1999a,b). Binned subsets of the radial RF data, limited in backazimuth and epicentral distance, were used as the input (observed) data. Events in any single bin subset varied no more than 20° in backazimuth and 15° in epicentral distance, although they usually varied much less than these maxima. Optimally, given a higher density and number of events, these bin sizes would be even smaller (e.g. ~5°–10°), to avoid attenuating *P<sub>s</sub>* phases (e.g. Cassidy 1992).

Loose *a priori* constraints were placed on the minimum and maximum *S*-wave velocities within each model velocity layer, as well as on the  $V_p/V_s$  ratio and the layer thicknesses.

Results from the non-linear inversion are shown in Fig. 4, for RF bins covering the backazimuth ranges 290°–310°, 310°–330° and 185°–200°. Fig. 4 presents density plots of the *S*-velocity model ensembles generated in the inversion. The lateral extent of the darkest grey areas in the figure provide an indication of how well the velocity structure is constrained by the data. Only a certain number (typically the best 100 to 300) of the generated models give an acceptable level of data fit to the observed RF waveforms. In the figure we plot the mean of the best 100 models. For the full ensemble of models there is also a single best-fitting model that generates the least misfit between the calculated and observed RFs (plotted as a dotted line for each solution ensemble in Fig. 4). However the useful information is really provided by the full ensemble of solutions, as described in Sambridge (1999a,b).

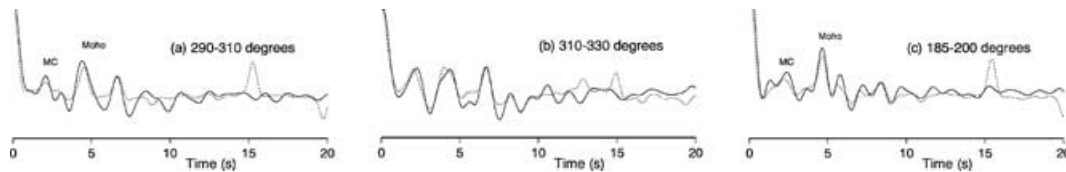


**Figure 5.** Calculated radial receiver function (light dashed line) using the best-fitting  $S$ -wave velocity model from the ensemble of model solutions, together with the observed binned receiver function (solid line) for VNDA station, for backazimuths (a) 290°–310° (b) 310°–330° (c) 185°–200°.  $P_s$  converted phases from the Moho and a Mid-crust (MC) discontinuity are labelled.

Each of the radial RFs shown in Fig. 5 were calculated using the single best-fitting model from the nonlinear inversion, to provide a means of waveform comparison with the observed RF. More than 100 other members of the model ensemble have similar levels of fit and so Fig. 5 can be regarded as reasonably representative of the match that can be achieved. On each of the examples the calculated phases (e.g.  $P_s$  from Moho) match the observed phases well (Fig. 5).

The derived velocity–depth profiles shown in Fig. 4 are well defined, but differ slightly for different backazimuth bins. For this station, as well as the other stations described below, we only present inversion results for a few of the backazimuth bins; bins which have appropriately low levels of energy on transverse RFs, and which contain RFs which do not rapidly change with backazimuth or epicentral distance.

Generally the VNDA profiles show  $S$ -wave velocities of 2.5 to 3.2 km s<sup>−1</sup> in the top 12 km, and a velocity increase at around 10 to 12 km depth. Fairly constant  $S$ -wave velocities of 3.4–3.8 km s<sup>−1</sup> are found in the mid-crust, although inversions for some backazimuths (e.g. ~320°) indicate a slight velocity reversal in the lower crust. Some of this variation may be due to structural dip, possibly on a mid-crustal discontinuity, as hinted by the observed features on the transverse RFs. The velocity gradient increases at 28–35 km depth, reaching mantle velocities (~4.1–4.3 km s<sup>−1</sup>) at ~34–35 km depth. These mantle velocities are poorly constrained by the RF data, as receiver functions are primarily sensitive to velocity contrasts and relative travel times, rather than absolute velocity (Ammon *et al.* 1990). With RF data there is an inherent trade-off between seismic velocity and layer thickness, although this non-uniqueness is reduced when surface multiples are present in the data, or when a range of incident slownesses can be utilized. This trade-off is apparent in Fig. 4, illustrated by the variation in  $S$ -wave velocity of the model ensemble, for any one depth. We note separately that although the  $V_p/V_s$  ratio is included as a parameter in the inversion, and is shown in the solutions (e.g. Fig. 4), the ratio is not well constrained in the inversion, and is not the focus of this study. The inclusion of the ratio serves primarily to allow for some of the effects of the sedimentary layer beneath the stations.

### 3.2 Central TAM, broad-band array stations

The quantity and quality of the waveform data derived from the temporary broad-band array stations are not comparable to the data derived for VNDA, primarily because of the short duration of the array deployment. However, a reasonable number of suitable teleseismic events were recorded by these stations. Receiver functions derived for 3 of the stations, AN08, AN09 and AN10 (Fig. 1b), are shown in Fig. 6. Velocity–depth profiles were also derived for these stations using the non-linear inversion technique, as described above for the VNDA data. The results are shown in Figs 7, 8 and 9.

At station AN09, which was located directly on basement rock, the  $P_s$  phase is very distinct at around 4–4.5 s (Fig. 6). The

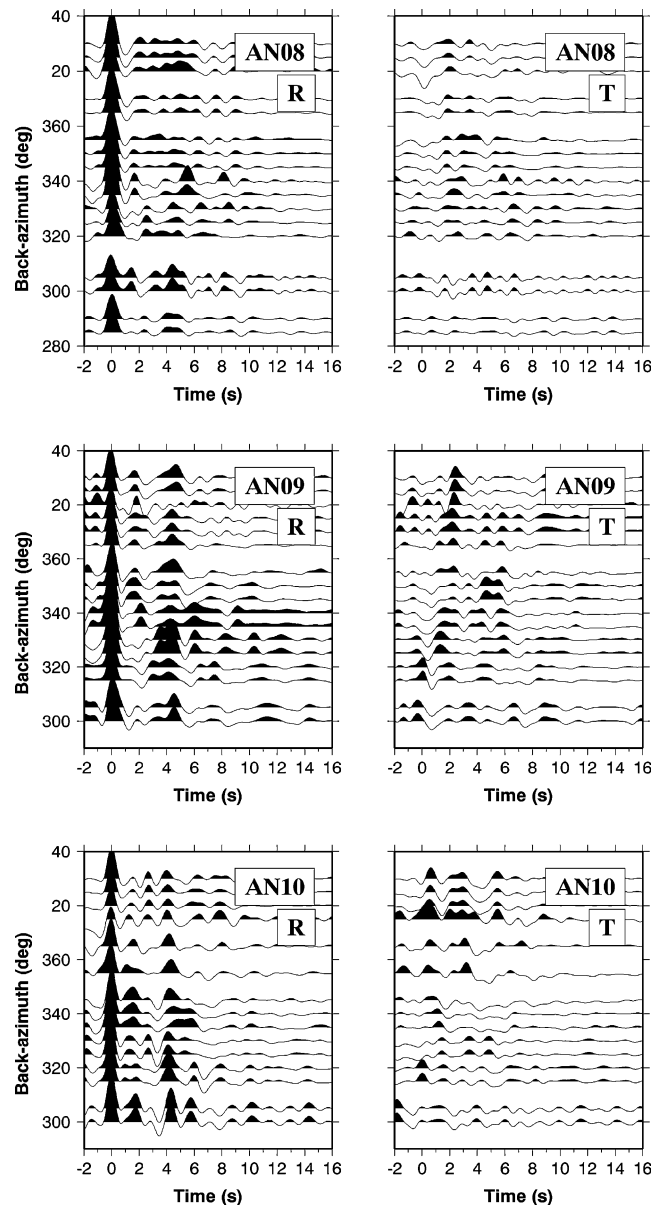


**Figure 6.** Radial receiver functions (left), and transverse receiver functions (right), plotted as a function of backazimuth, for stations AN08, AN09, and AN10. The  $P_s$  conversion from Moho (at 4–4.5 s time) is clear on the RFs from both AN09 and AN10, while it is weaker on AN08. A mid-crustal phase, at 1–2 s time, is clearly observed on the RFs for both AN09 and AN10.

phase appears slightly later (~4.5 s) for backazimuths from 25°–30°, and earliest (~4 s) at backazimuths of 320°–340°. The earlier mid-crustal phase seen on VNDA is seen for some but not all of the backazimuths on the RFs for station AN09, suggesting

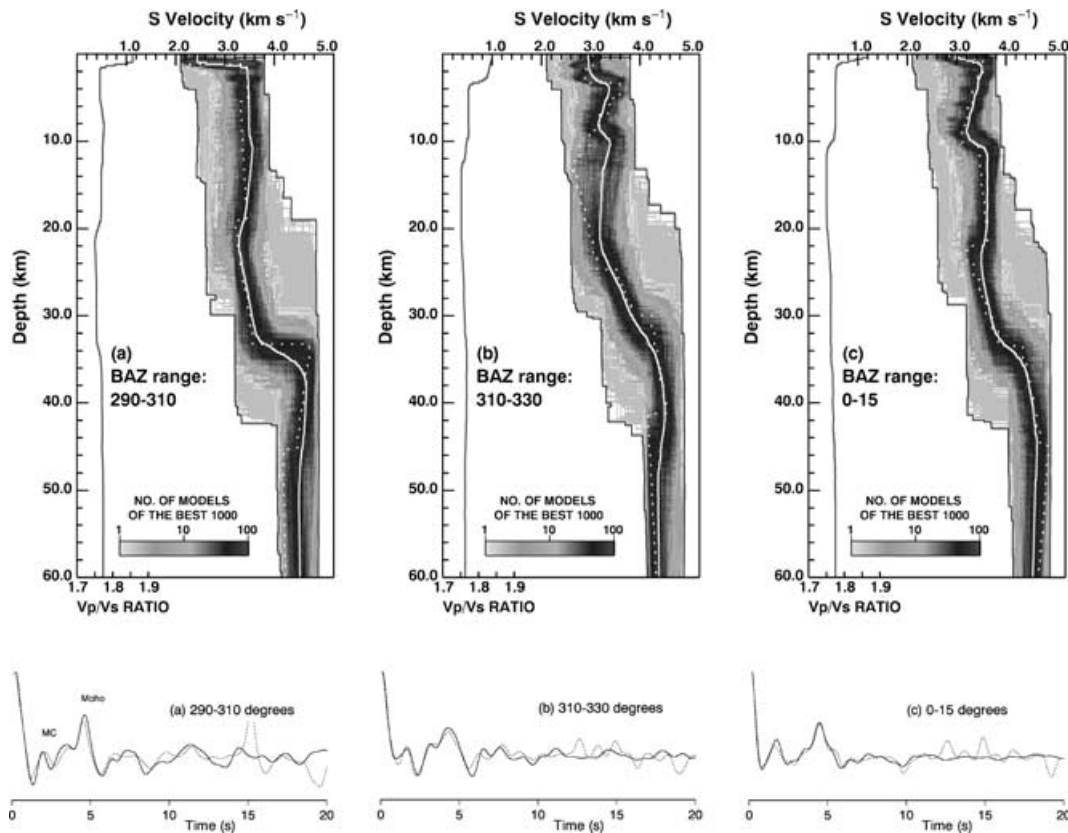


**Figure 7.** Seismic  $S$ -wave velocity models (top), and radial receiver functions (bottom), derived for station AN09, from non-linear inversion. The solid white line represents the mean of the best 100 models, and the dashed line represents the best of those models. Figure details are as shown in Figs 4 and 5. Results are shown for backazimuths (a)  $290^{\circ}$ – $310^{\circ}$ ; (b)  $310^{\circ}$ – $330^{\circ}$ ; (c)  $0^{\circ}$ – $15^{\circ}$ .

lateral variation of the crustal structure beneath the station. The inversion results (Fig. 7) for a backazimuth range of  $290^{\circ}$ – $310^{\circ}$  indicate a thin sedimentary layer, near-constant crustal velocities, and a well-defined Moho at  $\sim 33$ – $36$  km depth. The Moho  $P_s$  arrival seen in the observed RF bin (Fig. 7a) is well matched by the calculated RF, with a sharp  $P_s$  phase at  $\sim 4.5$  s. Similar characteristics are seen for other backazimuths (e.g. Figs 7b and c), for  $310^{\circ}$ – $330^{\circ}$  and  $0^{\circ}$ – $15^{\circ}$ ), although for these backazimuths a discontinuity is apparent in the mid-crust, at around 14 km depth. This discontinuity is clearly required for  $0^{\circ}$ – $15^{\circ}$  backazimuth, corresponding to the phase at  $\sim 1.5$  s on the observed RF.

Station AN10 (Fig. 1b) was located on Beacon Supergroup sediments, which overlie plutonic basement and metamorphic rocks of Precambrian to Ordovician age. The derived RFs (Fig. 6) show a clear  $P_s$  phase at 4–4.5 s time, especially for north-west backazimuths. A pulse is also observed at 1.0–1.5 s time (Fig. 6) for some backazimuths, slightly earlier than the similar pulse seen on the VNDA radial RFs. As for VNDA, we interpret this early pulse to represent a conversion from a mid-crustal discontinuity. Derived velocity–depth profile ensembles (Fig. 8) vary with event backazimuth, but they indicate the strong mid-crustal discontinuity at 8–12 km depth. Velocities are relatively constant below this discontinuity, down to 30–33 km depth, where Moho is also quite well defined, (as required by the clear  $P_s$  phases seen in the observed RFs).

Station AN08 is the western-most station of the array, located on Devonian siltstone (Pyne 1984), at the edge of the polar plateau (Fig. 1b). Beacon Supergroup sediments are more than 1.5 km thick beneath the station, overlying plutonic basement and metamorphic

rocks of Precambrian to Ordovician age (Isaac *et al.* 1995). The  $P_s$  phase on the observed RFs for AN08 (Fig. 6) is quite muted in comparison to that seen at the other stations, indicating that the Moho discontinuity beneath this station is not abrupt. Where the phase is visible (e.g. for  $290^{\circ}$ – $310^{\circ}$  backazimuth) the arrival time is about  $\sim 4.5$  s, indicating that the Moho is deeper than beneath other stations, or alternatively that the average crustal velocity beneath the station is slower. A low amplitude pulse is observed at 1.5–2 s time for some backazimuths, but is not very pronounced. Derived velocity–depth profiles, shown in Fig. 9, indicate a gentle velocity gradient through most of the crust, and a gradual transition between crustal and mantle velocities between 30 and 40 km depth. The Moho transition is clearly not abrupt, but is interpreted to lie between 36 and 40 km depth.

The data discussed above all show subtle changes in the arrival time of the Moho  $P_s$  phase beneath the TAM stations, indicating small lateral changes in the crustal structure beneath the TAM, which is also indicated by variability of the RFs with event backazimuth at individual stations. There are differences in the amplitude and character of the Moho and mid-crustal  $P_s$  phases between the stations, indicating spatial changes in the nature of the transition between the TAM crust and the upper-mantle, as well as in the mid-crustal discontinuity.

### 3.3 TAM coastline

Fig. 10 shows radial and transverse RFs derived for stations AN04 and AN05, which were located on the eastern side of the TAM, beside the Ross Sea coastline (Fig. 1b). The stations lie close to

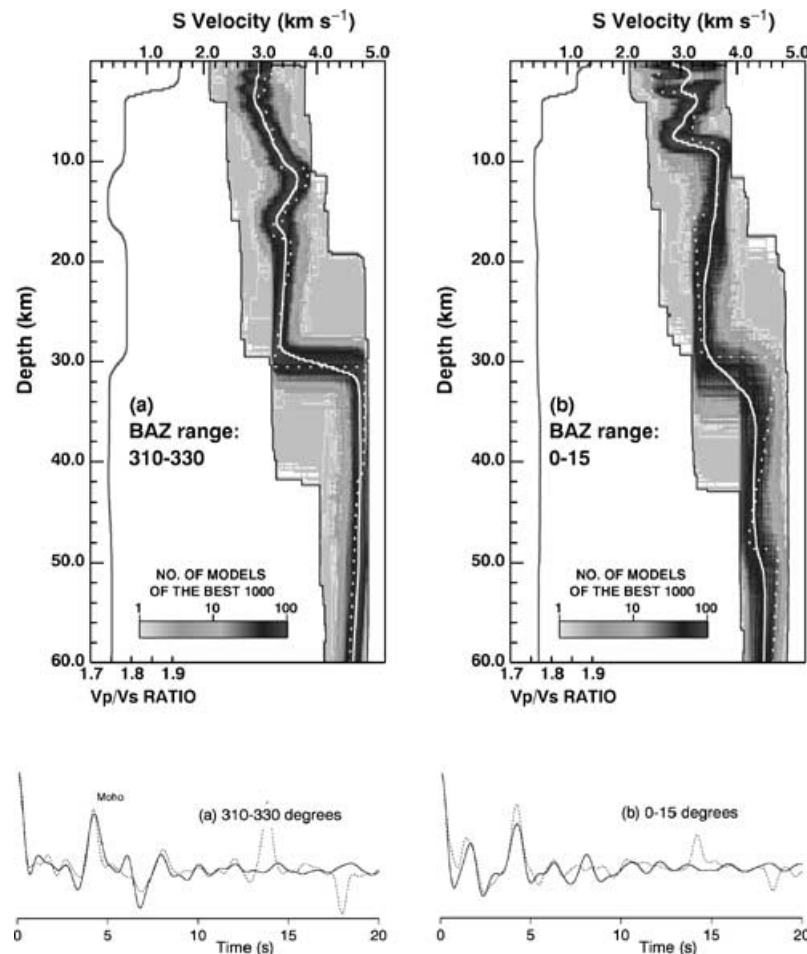


**Figure 8.** Seismic  $S$ -wave velocity models (top), and radial receiver functions (bottom), derived for station AN10, from non-linear inversion. The solid white line represents the mean of the best 100 models, and the dashed line represents the best of those models. Figure details are as shown in Figs 4 and 5. Results are shown for backazimuths (a)  $310^{\circ}$ – $330^{\circ}$ ; (b)  $0^{\circ}$ – $15^{\circ}$ .

the transition between the TAM and the VLB inferred by previous seismic and gravity studies (e.g. Hamilton *et al.* 2001). The teleseismic data recorded by these two stations are noisy compared to the data recorded inland, due to microseisms and scattering effects.

Data from station AN05 (Fig. 10) show a coherent pulse arrival at 2.0 to 2.2 s time across all backazimuths. Later, at  $\sim 4.8$ –5 s, there is a relatively weak and incoherent pulse. If we assume an average  $P$ -wave crustal velocity of between  $6.2$ – $6.8$  km s $^{-1}$ , and a Poisson's ratio of 0.25, then the depth of the discontinuity generating the 2.2 s pulse is  $\sim 18$ –21 km.

Results from the velocity–depth inversion for AN05 vary strongly with event backazimuth, but are shown in Fig. 11 for backazimuths  $270^{\circ}$ – $290^{\circ}$ ,  $338^{\circ}$ – $348^{\circ}$ , and  $0^{\circ}$ – $12^{\circ}$ . The velocity–depth profiles all indicate a strong velocity gradient between 10 and 20 km. We note that the solutions are not that well constrained, as illustrated for example by the range of velocities in the model ensemble at  $\sim 20$  km depth (Fig. 11a). Changes in the observed RFs with backazimuth, as well as the energy at 0 s time on the transverse RFs, suggests the presence of scattered energy, presumably associated with velocity heterogeneity beneath and near the station. Mantle velocities appear to be reached at around 18–20 km depth (Fig. 11). Similar Moho-depths, of 21–23 km, have been interpreted from reflection seismic data just east of this station (McGinnis *et al.* 1985). Our results

imply that the thin crust found by McGinnis *et al.* extends to, and beneath, the TAM coastline.

The data for AN04, shown in Fig. 10, are noisier and less coherent than for AN05, with higher energy levels on the transverse component (Fig. 10), probably resulting from near-receiver scattering associated with crustal heterogeneity. The data distribution with respect to backazimuth is also quite sparse. Due to the level of transverse energy, and the variability of the RFs with backazimuth, non-linear inversion for 1-D velocity structure was not attempted for this station.

### 3.4 Other array stations in the TAM

We have chosen not to present receiver function data from stations AN02, AN06, AN07 and AN14, which had high microseism noise or instrumental problems that affected the quality of derived RFs.

### 3.5 Ross Island region, West Antarctica

Fig. 12 shows stacked RFs derived for station SBA, located on the coastline of Ross Island (Fig. 1b), which is situated at the south end of the Terror Rift. There is present-day active volcanism at Mt Erebus, in the centre of Ross Island, just north-east of SBA (LeMasurier 1990). Gravity data and multichannel seismic data

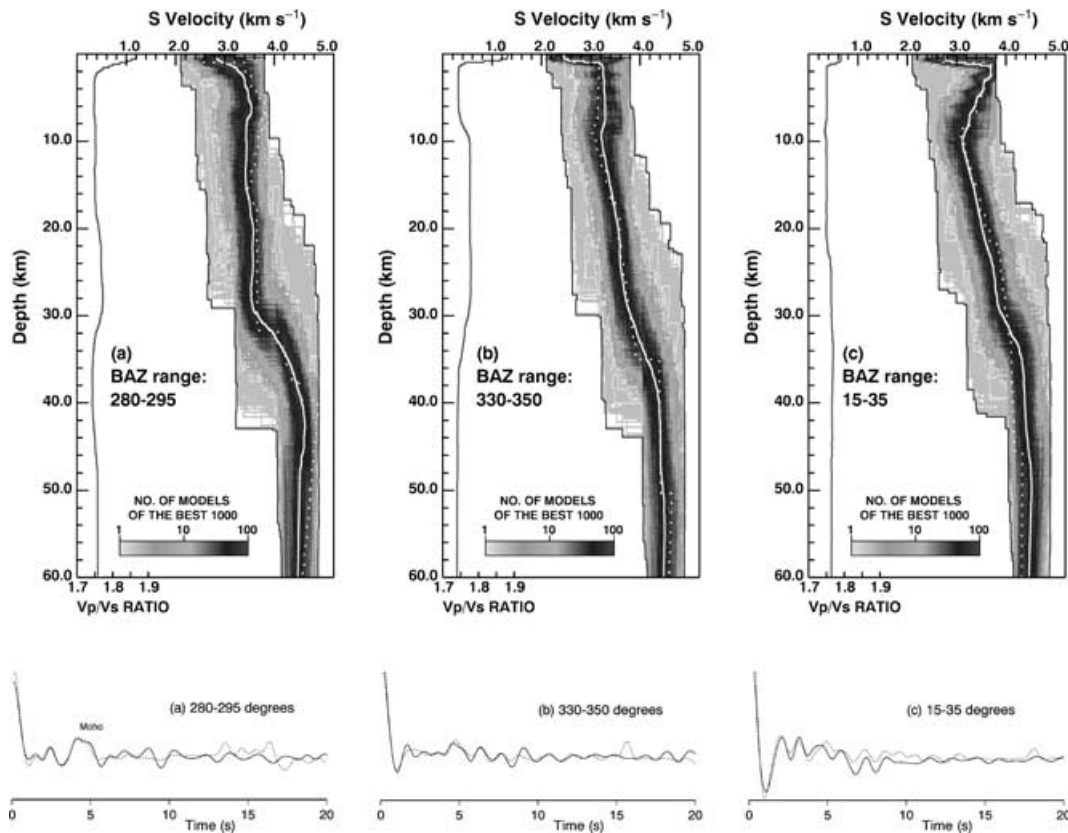


**Figure 9.** Seismic *S*-wave velocity models (top), and radial receiver functions (bottom), derived for station AN08, from non-linear inversion. The solid white line represents the mean of the best 100 models, and the dashed line represents the best of those models. Figure details are as shown in Figs 4 and 5. Results are shown for backazimuths (a) 280°–295°; (b) 330°–350°; (c) 15°–35°.

interpretations indicate an average crustal thickness of 18–21 km in the Ross Sea (e.g. Cooper *et al.* 1997; Trey *et al.* 1997). Cooper *et al.* (1997) found evidence of crustal thinning beneath the eastern flank of the VLB, just north-east of Ross Island, with high velocities ( $\sim 7.9 \text{ km s}^{-1}$ ), possibly representing mantle, at  $\sim 17$ –18 km depth. At shallower depths, multichannel seismic data indicates a large thickness of sediments near Ross Island (e.g. McGinnis *et al.* 1985; Cooper *et al.* 1987).

Radial RFs derived from the SBA data (Fig. 12), are very complex in the first 3 s, with a large amplitude pulse 0.5–1.5 s after the direct *P* arrival. We interpret this large pulse to represent a *Ps* converted pulse from the bottom of a thick deposit of low-velocity sediments. Where the sedimentary layer is thinner interference of the *Ps* conversion and the direct *P* arrival produce a composite peak which is shifted in time from 0 s. Reverberations inside the sedimentary layers contribute to the pulse complexity over 1–3 s. Very similar complex RF effects have been observed above other shallow sedimentary basins (e.g. Shibutani *et al.* 1996; Clitheroe *et al.* 2000b; Sheehan *et al.* 1995) and caldera fill (Ligorria & Ammon 1999).

The nature of the complex pulse varies considerably with event backazimuth. This variation with backazimuth is expected, given that the sedimentary basins around and beneath Ross Island vary considerably in thickness and geometry (McGinnis *et al.* 1985; Cooper *et al.* 1987). Receiver functions derived for event backazimuths between 285°–360° are all quite similar, with a weak direct-*P* pulse, a strong pulse at 1.5 s, a clear coherent negative pulse at 3.5 s, and a pulse at 3.9–4 s, followed by reverberations at 5–6 s and 7–8 s.

RFs for event backazimuths 0°–22° have a stronger pulse at 1 s time, but retain complexity in the first 3 s, while RFs for backazimuths 80°–140°, from the east-southeast, have a broad complex arrival in the first 3 s followed by a negative pulse at 3 s. These changes in the observed RFs with backazimuth indicate lateral changes in the sedimentary thickness, sedimentary velocities, and basement conditions near the station.

The potential effect of a shallow sedimentary layer can be examined using forward synthetic modelling. We created several synthetic radial RFs using a variety of 1-D velocity models, involving a simple 2-layer crust, as well as involving sedimentary layers (Fig. 13). A Poisson's ratio of 0.25 was assumed for all of the modelling. Fig. 13(a) represents the calculated effect of a simple 2-layer crust with a Moho at 18 km depth. The synthetic RF shows a *Ps* phase at 2.2 s and a *PpP<sub>m</sub>s* phase at 7.6 s (Fig. 13a). Fig. 13(b) uses the same crustal thickness, but also includes a 1-km thick sedimentary layer. The synthetic RF is more complex than that derived for (a), and the first pulse has a visible phase delay. As we increase the thickness of the sedimentary layer to 2-km, 3-km and 4-km (Figs 13c, d and f respectively) the effect of the sedimentary layer on the RF becomes quite marked. Strong pulses develop at 1–2 s time, and the initial pulse at  $\sim 0$  s becomes complex. The synthetic functions (c)–(e) show very similar characteristics to some of the observed RFs seen for both stations SBA and AN01 (described below). Comparing Figs 13(c) and (e) to Fig. 13(a), it is clear that the conversions and reverberations associated with the surface sedimentary layers can potentially overwhelm the *Ps* conversion from the Moho discontinuity.



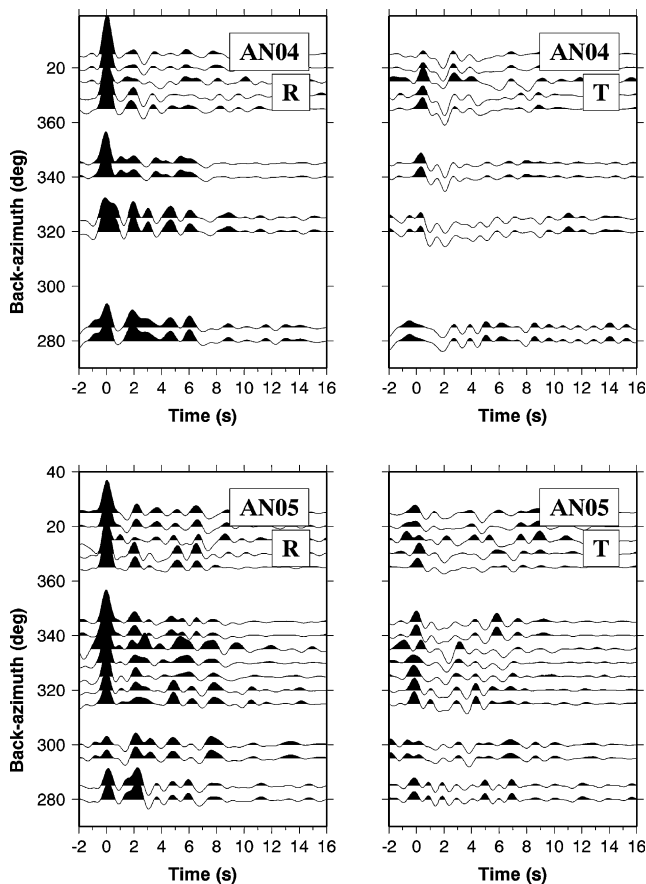


**Figure 10.** Radial (left) and transverse (right) receiver functions, plotted as a function of backazimuth, for stations AN04 and AN05. The RFs from station AN05 show a coherent phase at  $\sim 2$  s across all backazimuths, which is inferred to represent the Moho  $P_s$  conversion.

Results of non-linear inversion of the observed RF data from SBA are shown in Fig. 14, for the backazimuth range  $280^\circ$ – $300^\circ$ . Low  $S$ -wave velocities are found down to more than 5 km depth (Fig. 14), commensurate with velocities expected for sedimentary deposits. A high  $S$ -wave velocity gradient is required between the surface and  $\sim 14$  km depth. The depth of the Moho discontinuity cannot readily be distinguished although mantle velocities appear to be reached by 20 km depth.

Station AN01 was located on the northern tip of Ross Island, to the north of SBA (Fig. 1b). The radial RFs derived from station AN01 data (Fig. 15), are similar to those derived for SBA, although they appear less complex. A secondary pulse is seen at 2–2.5 s, for all backazimuths. The RFs from  $120^\circ$ – $135^\circ$  backazimuth show a strong, clean, direct  $P$  pulse with no phase lag, and then a clear second pulse at 2.5 s. As there appears to be little effect from sedimentary layers for this backazimuth, this 2.5 s pulse is inferred to represent the  $P_s$  conversion from the Moho discontinuity. The velocity–depth profile obtained for station AN01 for this backazimuth range (Fig. 16) indicates a high velocity–depth gradient in the top 20 km, but not as extreme as required for other backazimuths, or as high as required for station SBA. Mantle velocities are reached at around 19–21 km depth. Velocity–depth profiles derived for other backazimuths require the presence of a significant thickness of low-velocity sediments, as suggested by the complexity of the observed RFs.

## 4 DISCUSSION

### 4.1 Moho depths beneath Ross Island, West Antarctica

Our results, summarized in Fig. 17, indicate that the crust is  $\sim 19$ – $21$  km thick beneath station AN01, at the northern tip of Ross Island. This estimated crustal thickness is in general agreement with results from seismic reflection and refraction surveys offshore in the western and central Ross Sea region (e.g. Cooper *et al.* 1987; Cooper *et al.* 1997). Just northeast of Ross Island Cooper *et al.* (1997) reported crustal thicknesses of 17–18 km beneath the southern Central trough, and 21–24 km beneath the flanking ridges of the trough. Below the sedimentary section they interpreted 2 separate crustal layers, with a  $P$ -wave velocity of  $5.8$ – $6.4$  km  $s^{-1}$  in the upper crust,  $6.5$ – $7.1$  km  $s^{-1}$  in the lower crust, and  $7.9$  km  $s^{-1}$  in the upper-mantle. These seismic observations are also consistent with gravity interpretations (e.g. Davey & Cooper 1987) which indicate a crustal thickness of 23 km beneath most of the VLB, apart from along the western side of McMurdo Sound (i.e. just north of station AN05) where a slightly shallower Moho depth is required (Davey & Cooper 1987).

### 4.2 Transition between East and West Antarctica

Multichannel seismic data from offshore station AN02 (Fig. 1b) show NW and NNW striking faults near the TAM coastline, parallel to the Transantarctic Mountains (Hamilton *et al.* 2001). Taken together with similar faults inferred by Barrett *et al.* (1995) and Hamilton *et al.* (2001) recognized this fault set as a major feature controlling the uplift of the TAM, and named it the McMurdo Sound Fault Zone (MSFZ, Fig. 17). Immediately west of this fault zone the receiver function data from station AN05 indicate a crustal thickness of  $\sim 16$ – $20$  km (Fig. 17), with a strong velocity gradient between 10 and 20 km depth. However, the RF data from station AN10, just 25 km west of station AN05, indicate a crustal thickness of  $\sim 30$ – $33$  km, and a strong mid-crustal discontinuity at  $\sim 10$  km depth, a markedly different crustal structure from that beneath AN05, indicating a relatively sharp change in the crustal thickness and composition between the two stations (Fig. 17).

The nature of the crustal transition along the margin between the VLB and the TAM has previously been inferred using gravity data (Davey & Cooper 1987). The data indicate a rapid change in crustal thickness, from  $\sim 20$  to  $\sim 40$  km, between the VLB and the TAM at the latitude corresponding to station AN02 (Fig. 1b). Further south, near station AN05 at  $77.7^\circ$  S latitude, the observed gravity gradient is gentler near the coastline (Smithson 1972; Davey & Cooper 1987). Our RF data from AN05 indicates that the crust beneath this section of the coastline is still relatively thin, and that the transition to thicker TAM crust must occur west of station AN05.

There are only a few other geophysical studies that have provided information on the TAM crust and the transition between the VLB and the TAM. Up in the vicinity of Mt. Melbourne, in northern Victoria Land, a gentle crustal transition between the VLB and the TAM was inferred from gravity data (Redfield & Behrendt 1992) as well as from offshore-onshore seismic data recorded by O'Connell & Stepp (1993). The seismic data indicate that the depth to seismic Moho is 22 km beneath the coastline at that location, thickening to 26 km at a position 30 km inland from the coast. To the south of that experiment, at  $76^\circ$  S latitude, receiver function observations by Pondrelli *et al.* (1997) indicate Moho at a depth of around 25 km near the coastline, with an average Moho dip of about  $15^\circ$ . Similar crustal thicknesses have been interpreted from seismic wide-angle

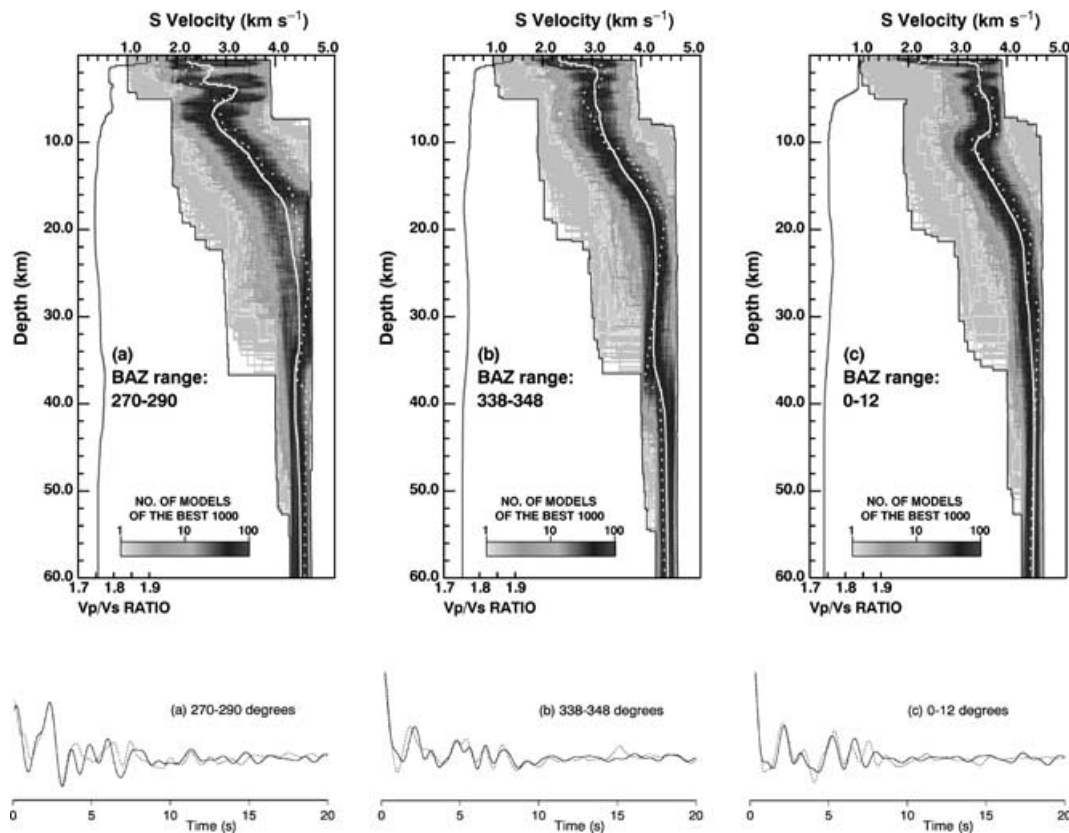


**Figure 11.** Seismic  $S$ -wave velocity models (top), and radial receiver functions (bottom), derived for station AN05, from non-linear inversion. The solid white line represents the mean of the best 100 models, and the dashed line represents the best of those models. Figure details are as shown in Figs 4 and 5. Results are shown for backazimuths (a)  $270^{\circ}$ – $290^{\circ}$ ; (b)  $338^{\circ}$ – $348^{\circ}$ ; (c)  $0^{\circ}$ – $12^{\circ}$ .

refraction data recorded in the same vicinity (Della Vedova *et al.* 1997).

Well to the south of Ross Island, in the vicinity of the Robb Glacier at  $82^{\circ}\text{S}$ , wide-angle reflection and refraction seismic data recorded during the SERIS experiment delineated the transition between East and West Antarctica (ten Brink *et al.* 1993; Bannister *et al.* 1999b). The SERIS seismic and gravity data show the crust thickening from 22 km beneath the Ross Ice Shelf, to between 30 and 35 km beneath the TAM, in a transition zone  $\sim 40$  km wide, which begins 10–20 km inland of the TAM mountain front. Although the SERIS seismic line crossed the TAM Front in an area of the TAM that has undergone at least 5 km of uplift, the interpreted sedimentary and deeper crustal structure immediately to the east of the TAM Front is relatively flat and undeformed (ten Brink *et al.* 1993), conflicting with expectations from isostatic and mechanical models of rift formation (e.g. Stern & ten Brink 1989).

#### 4.3 TAM velocity and crustal structure

Beneath the TAM our RF data indicate that the crustal thickness is  $\sim 33$ – $36$  km beneath VNDA station (Fig. 17), thickening further to the west beneath station AN08 (Fig. 17) to 36–40 km. The RF data also clearly requires the presence of a  $\sim 8$ – $14$  km thick upper crustal layer beneath VNDA, and AN10, with a strong velocity discontinuity at the base of this upper crustal layer. In comparison there is no evidence for a separate upper crustal layer beneath station AN08 on the western side of the TAM. Instead there is a gentle velocity gradient between the surface and Moho, with a slight increase in

the gradient with depth. Station AN08 lies close to the boundary between two lower crustal provinces (the Miller Range Block and Beardmore Glacier Block) interpreted by Borg & DePaolo (1990), inferred on the basis of isotopic compositions.

At the base of the lower crust the transition between crustal and mantle velocities changes in nature beneath the different stations. The transition appears to be abrupt beneath stations AN10 and VNDA, but quite gradational beneath the eastern-most station, AN08. A similar gradational Moho is also observed below the axis of the Tasman Fold Belt of Australia (Shibutani *et al.* 1996), which lay north of the Transantarctic Mountains before Gondwana breakup (e.g. Veevers & Eittreim 1988). In that region Clitheroe *et al.* (2000a) note that the broad Moho transition is consistent with formation models involving underplating. In the TAM region additional data density is really required, to allow for 2-D dipping structural effects, before similar interpretations can confidently be made.

The crustal thickness beneath the TAM has previously been inferred at  $\sim 40$ – $43$  km, using thermobarometry of granulite inclusions (Berg *et al.* 1989), while early gravity interpretations also indicated a crustal thickness of  $\sim 40$  km in this region (Smithson 1972). Our interpretations of the RF data are generally consistent with these crustal thicknesses. Similar crustal thicknesses of  $\sim 41$ – $43$  km have been found to the north, at  $76^{\circ}\text{S}$  latitude, using receiver function analysis, between 125 and 160 km from the coastline (Pondrelli *et al.* 1997). Refraction data recorded in the same region during the ACRUP offshore-onshore seismic experiment (Fig. 1b), indicate a crustal thickness thickening from 25 km beneath the coast to  $\sim 38$  km beneath the TAM (Della Vedova *et al.* 1997).

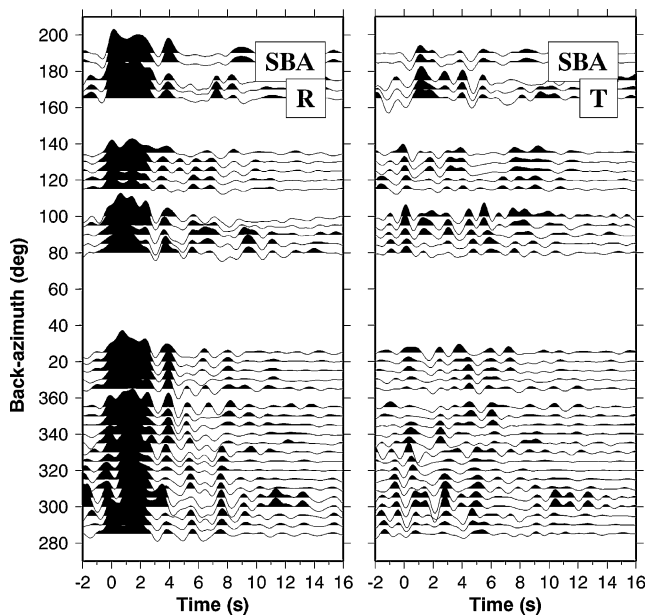


**Figure 12.** Radial (left) and transverse (right) receiver functions, plotted as a function of backazimuth, for station SBA. The RFs are complex in the first 2–3 s, and the initial phase, at 0-s, displays a phase shift indicative of the effects of shallow sediments. A coherent negative pulse is seen at 3–3.5 s time.

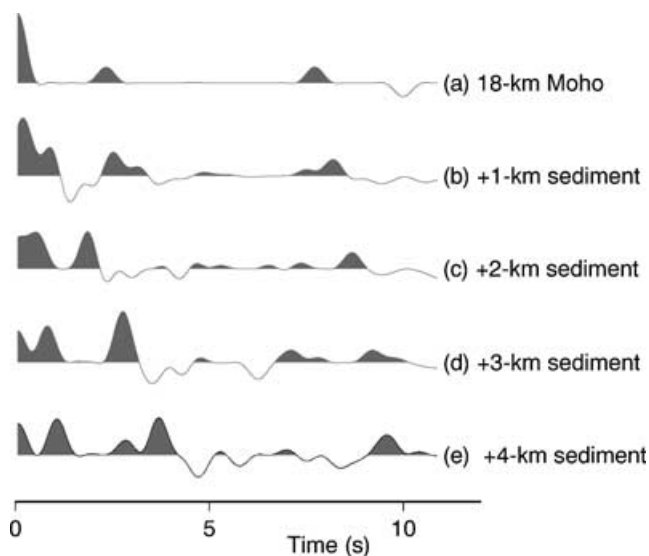


**Figure 13.** Synthetic radial receiver-functions derived for several velocity models. (a) 18-km Moho with no sediments; (b) as for (a), but with 1-km of sediment with  $V_p = 3 \text{ km s}^{-1}$ ; (c) as for (a), but with 2-km of sediment; (d) as for (a), but with 3-km of sediment; (e) as for (a), but with 4-km of sediment.

Various uplift mechanisms have been suggested for the TAM, including simple shear extension (Fitzgerald *et al.* 1986), and thermal conduction or advection, together with erosional and isostatic forces (Stern & ten Brink 1989; ten Brink & Stern 1992). In the latter models the uplift of the TAM scarp is assisted by thermal conduction of heat from the West Antarctic Rift System to the older, thicker, lithosphere west of the TAM Front, which requires that regional thermal anomalies are present in the upper-mantle immediately beneath the TAM Front. New results from the Cape Roberts drilling

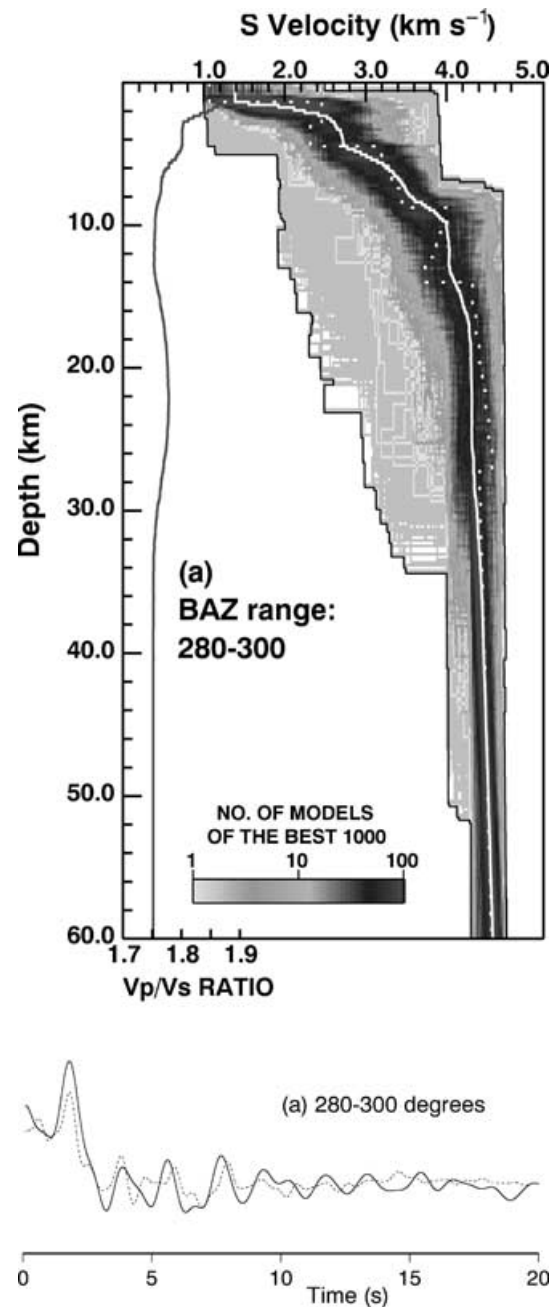


**Figure 14.** Seismic  $S$ -wave velocity models (top) and calculated radial receiver functions (bottom) derived for station SBA, from non-linear inversion. The solid white line represents the mean of the best 100 models. A substantial thickness of low velocity sediment is required in the top few kilometres, and the Moho is poorly defined.

project however indicate that the formation of the VLB in the Ross Sea began  $\sim 34 \text{ Ma}$ , later than previously thought (Cape Roberts Science Team 2000). The main period of TAM uplift which began at  $\sim 55 \text{ Ma}$ . (Fitzgerald 1992) thus preceded, by about 20 Ma, the formation of the VLB, implying that the TAM uplift is not necessarily coupled with the rift development of the VLB. Further south, as mentioned above, SERIS seismic data show relatively undeformed sedimentary structure beneath the Ross Ice Shelf immediately adjacent to the TAM Front, rather than the down-warpage expected from the conceptual Vening Meinesz rift model (Heiskanen & Vening Meinesz 1958). Stern *et al.* (1992), noting the SERIS results,

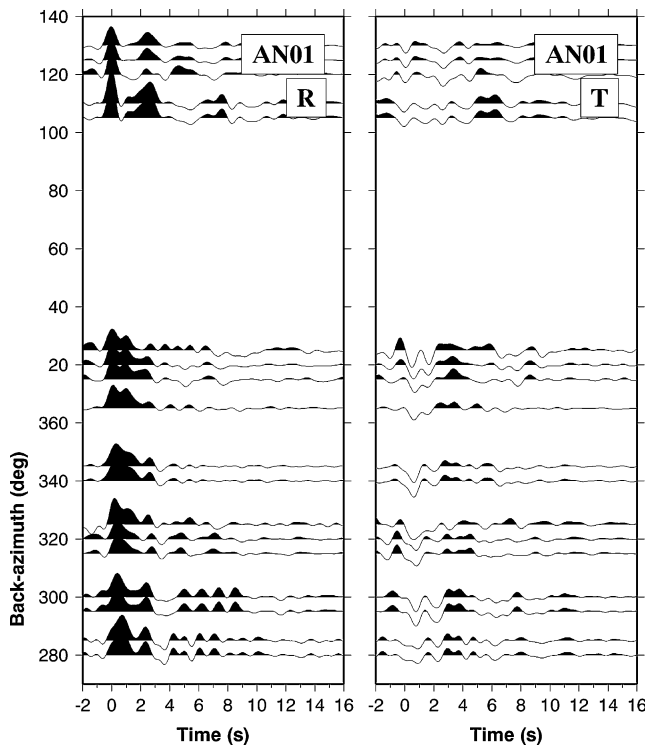


**Figure 15.** Radial (left) and transverse (right) receiver functions, plotted as a function of backazimuth, for station AN01. A coherent clear phase is observed at 2–2.5 s across RFs for 110–140 degrees backazimuth. At other backazimuths the initial 0-s phase exhibits a phase shift indicative of the effect of thick sedimentary layers.

suggest that a mechanism involving isostatic Vening Meinesz uplift might not be as dominant as that of thermal uplift and the subsequent effects of glacial erosion, while ten Brink *et al.* (1997) hypothesize that the main uplift phase of the TAM was not related to extension in the Ross Sea, but rather to minor trans-tensional movement between East and West Antarctica in the early Tertiary. The presence of such a trans-tensional boundary does not require the existence of rift basins along the entire mountain front, and is also still in agreement with the observed lateral variations in crustal thickness. Our data from the present study do not at this stage provide any strong evidence to refute or support the models for TAM uplift, apart from indicating that the crust is relatively thin close to the McMurdo Sound Fault Zone on the east side of the TAM, and that the crustal thickness and composition changes quite rapidly between station AN05 and station AN10 beneath the TAM.

## 5 CONCLUSIONS

Receiver function analyses of recorded teleseismic waveforms indicate large lateral changes in velocity structure beneath the Transantarctic Mountains and Ross Island, reflecting the nature of the crustal transition between West and East Antarctica.

The crustal thickness inferred beneath Ross Island, West Antarctica, is 19–21 km, consistent with previous estimates derived from multichannel seismic reflection and refraction experiments. Further west, immediately adjacent to the large fault zone inferred to have controlled the uplift of the TAM, the crustal thickness is estimated to be ~16–20 km. Further inland, beneath the TAM, the estimated Moho depths range from 30–33 km (~30 km from the coast) to 36–40 km (~85 km from the coast), deepening away from the coast.

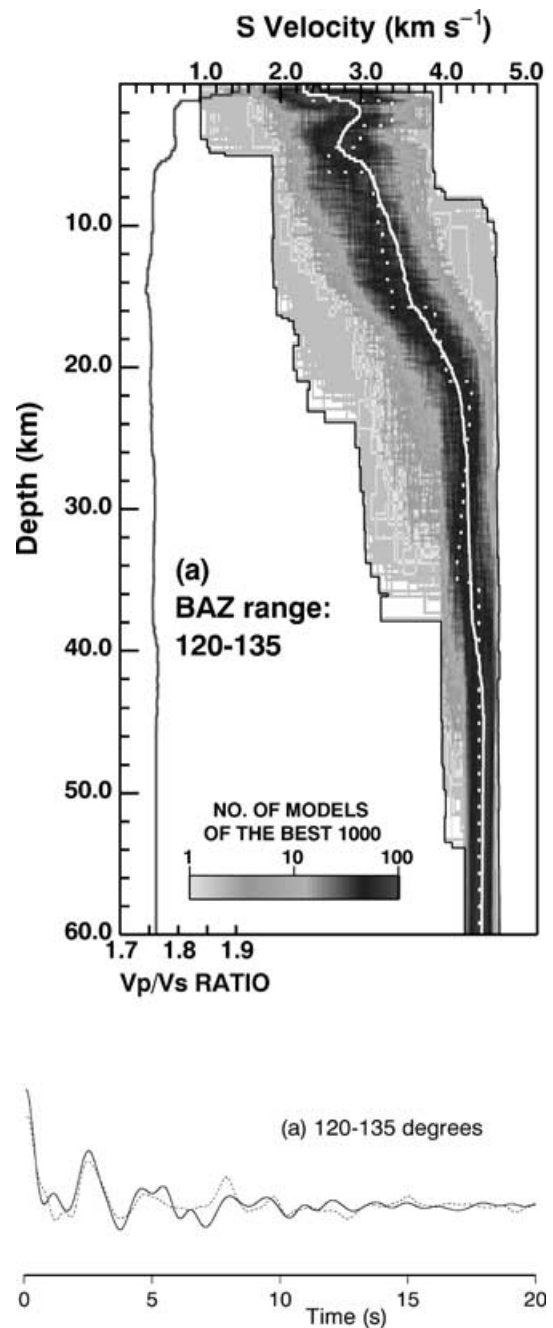


**Figure 16.** Seismic *S*-wave velocity models (top), and radial receiver functions (bottom), derived for station AN01, from non-linear inversion. The solid white line represents the mean of the best 100 models, and the dashed line represents the best of those models. Figure details are as shown in Figs 4 and 5. Results are shown for backazimuths 120°–135°. Mantle velocities are reached at around 19–21 km depth.

These results are in broad agreement with previous seismic and gravity interpretations. Further RF data are required to help define the nature of the crustal transition close to the TAM Front, in order to assist discrimination between the various proposed models of TAM uplift. Data from the current TAMSEIS deployment (Wiens *et al.*, 1993) may help in this respect.

Beneath the TAM we note the presence of a mid-crustal discontinuity at ~8–14 km depth. This discontinuity is more pronounced beneath the eastern-most stations and absent on the western side

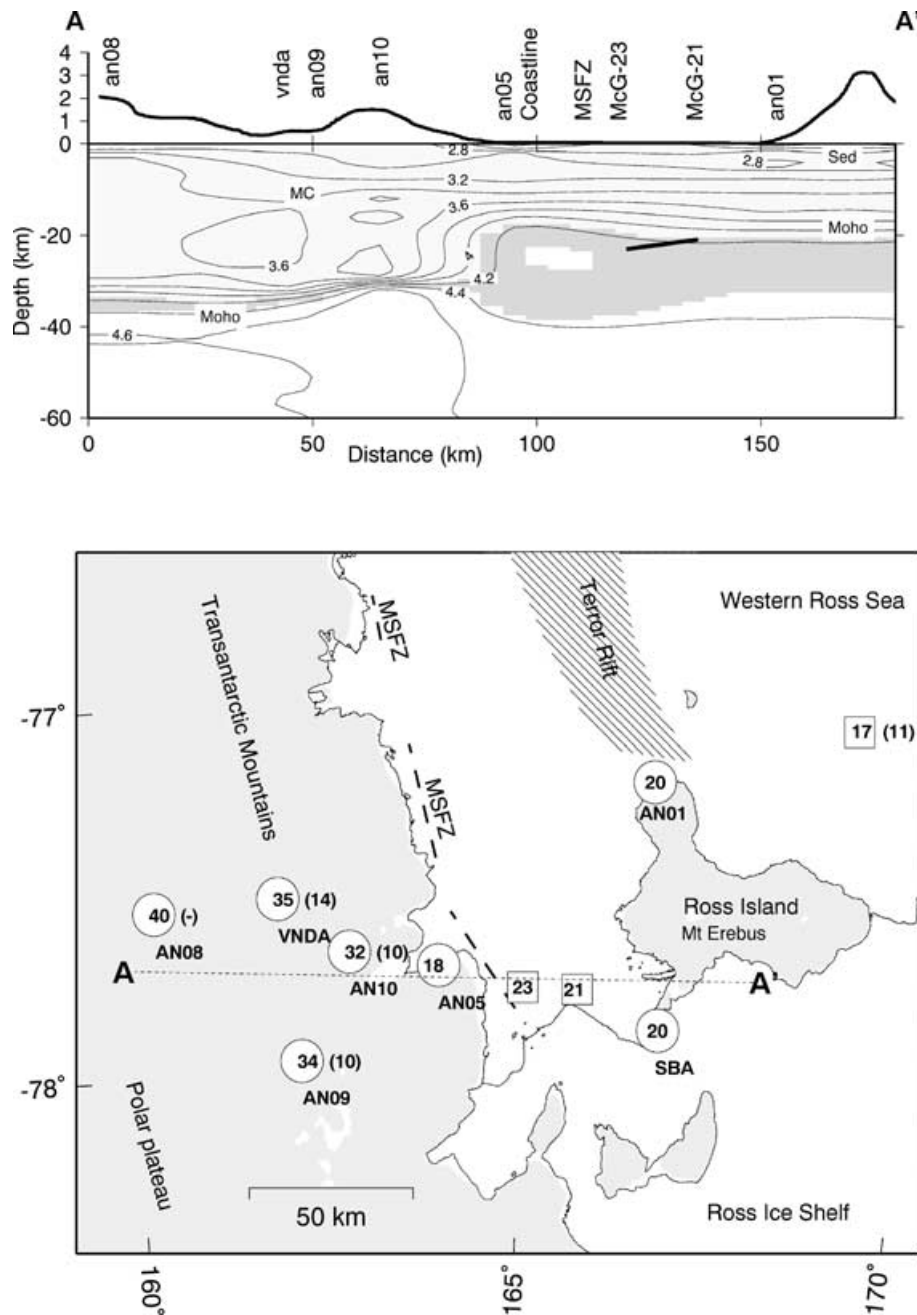


**Figure 17.** (a) Schematic cross-section of the crust across the region, showing smoothed  $S$ -wave velocity as a function of depth. Surface topography (in km) is shown vertically exaggerated. The black bar shows the Moho-depth estimates of McGinnis *et al.* (1985). (b) Approximate inferred depth of the Moho (inside open circles) and the mid-crustal-discontinuity (inside brackets) estimated from the non-linear inversion of the receiver function data. The Moho depths previously estimated from multichannel seismic reflection data (McGinnis *et al.* 1985; Cooper *et al.* 1997) are shown inside open boxes.

of the TAM, indicating spatial changes in the composition of the mid and lower crust beneath the mountains, which has also been inferred from geochemical analyses. Data further away from the present study area, e.g. to the south, will help to confirm these changes in the mid-crustal discontinuity and the association with lower crustal provinces.

## ACKNOWLEDGMENTS

We would like to thank Malcolm Sambridge for the use of his NA software, Peter Goldstein for use of SAC2000 analysis code

(Goldstein *et al.* 1999), and Jeffrey Park and Vadim Levin for their multi-taper correlation routines. Broad-band array seismometers and recorders were provided by the Australian National Seismic Imaging Resource (ANSIR), and field support in Antarctica was provided by Antarctica New Zealand. We acknowledge use of data from Vnda and SBA stations, which are maintained and operated by the USGS Albuquerque Seismological Laboratory. The Foundation of Research, Science and Technology provided financial support through FRST contract C05523. We also thank Ken Gledhill, Mike Hagerty and an anonymous reviewer for their helpful suggestions.

## REFERENCES

- Ammon, C.J., 1991. The isolation of receiver effects from teleseismic P waveforms, *Bull. seism. Soc. Am.*, **81**, 2504–2510.
- Ammon, C.J., Randall, G.E. & Zandt, G., 1990. On the nonuniqueness of receiver function inversions, *J. geophys. Res.*, **95**, 15 303–15 318.
- Bannister, S., Snieder, R.K. & Passier, M.L., 1999a. Shear-wave velocities under the Transantarctic Mountains and Terror Rift from surface wave inversion, *Geophys. Res. Lett.*, **27**, 281–284.
- Bannister, S., Melhuish, A., Henrys, S., Stern, T. & ten Brink, U., 1999b. Deep seismic reflections beneath the Trans-Antarctic Mountain Front, from reprocessed SERIS seismic data, *Terra Antarctica*, **6**, 363–364.
- Barrett, P.J., Henrys, S.A., Bartek, L.R., Brancolini, G., Busetti, M., Davey, F.J., Hannah M.J. & Pyne, A.R., 1995. Geology of the margin of the Victoria Land Basin off Cape Roberts, southwest Ross Sea, in *Geology and Seismic Stratigraphy of the Antarctic Margin*, *Antarc. Res. Ser.*, **68**, pp. 183–207, eds Cooper, A.K., Barker, P.F. & Brancolini, G., AGU, Washington, DC.
- Behrendt, J.C., LeMasurier, W.E., Cooper, A.K., Tessensohn, F., Trehu, A. & Damaske, D., 1991a. Geophysical studies of the West Antarctic Rift System, *Tectonics*, **10**, 1257–1273.
- Behrendt, J.C., Duerbaum, H.J., Damaske, D., Saltus, R., Bosum, W. & Cooper, A., 1991b. Extensive volcanism and related tectonism beneath the Ross Sea continental shelf, Antarctica: Interpretation of an aeromagnetic survey, in *Geological Evolution of Antarctica*, pp. 299–304, eds Thompson, M.R.A., Crame, J.A. & Thomson, J.W., Cambridge University Press, Cambridge, UK.
- Berg, J.H., Moscati, R.J. & Herz, D.L., 1989. A petrologic geotherm from a continental rift in Antarctica, *Earth planet. Sci. Lett.*, **93**, 98–108.
- Blackman, D.K., Von Herzen, R.P. & Lawver, L.A., 1987. Heat flow and tectonics in the western Ross Sea, Antarctica, in *The Antarctic Continental Margin: Geology and Geophysics of the Western Ross Sea*, *Earth Science Series*, Vol. 5B, pp. 179–189, eds Cooper, A.K. & Davey, F.J., Houston, Texas, Circum-Pacific Council for Energy and Natural Resources.
- Borg, S.G. & DePaolo, D.J., 1990. Crustal basement provinces of the Transantarctic Mountains, Ross Sea sector, *Antarctic Journal of the U.S.*, **25**, 29–31.
- Bott, M.H.P. & Stern, T.A., 1992. Finite element analysis of Transantarctic Mountain uplift and coeval subsidence in the Ross Embayment, *Tectonophysics*, **201**, 341–356.
- Cape Roberts Science Team, 2000. Studies from Cape Roberts Project. Initial Report on CRP-3, Ross Sea, Antarctica, *Terra Antarctica*, **7**, 1–209.
- Cassidy, J.F., 1992. Numerical experiments in broadband receiver function analysis, *Bull. seism. Soc. Am.*, **82**, 1453–1474.
- Clietheroe, G., Gudmundsson, O. & Kennett, B.L.N., 2000a. The crustal thickness of Australia, *J. geophys. Res.*, **105**, 13 697–13 713.
- Clietheroe, G., Gudmundsson, O. & Kennett, B.L.N., 2000b. Sedimentary and upper crustal structure of Australia from receiver functions, *Aust. J. Earth. Sci.*, **47**, 209–216.
- Cooper, A.K., Davey, F.J. & Behrendt, J.C., 1987. Seismic stratigraphy and structure of the Victoria Land Basin, Western Ross Sea, Antarctica, in *The Antarctic Continental Margin: Geology and Geophysics of the Western Ross Sea*, Vol. 5B, pp. 27–76, eds Cooper A.K. & Davey, F.J., Earth Science Series, Houston, Texas, Circum-Pacific Council for Energy and Natural Resources.
- Cooper, A.K., Trey, H., Pellis, G., Cochran, G., Egloff, F., Busetti, M. & ACRUP Working Group, 1997. Crustal structure of the southern Central Trough, Western Ross Sea, in *The Antarctic Region: Geological Evolution and Processes*, pp. 637–642, ed. Ricci, C.A., Terra Antarctica Publication, Siena.
- Davey, F.J. & Cooper, A.K., 1987. Gravity studies of the Victoria Land Basin and Iselin Bank, in *The Antarctic Continental Margin: Geology and Geophysics of the Western Ross Sea*, Vol. 5B, pp. 119–137, eds Cooper, A.K. & Davey, F.J., Earth Science Series, Houston, Texas, Circum-Pacific Council for Energy and Natural Resources.
- Davey, F.J. & Woodward, R., 1995. The seismological and geomagnetic observatories at Scott Base and Vanda, McMurdo Sound, Antarctica, 1995, *VII International Symposium on Antarctic Earth Sciences: Siena (Italy)*, 10–15 September 1995: abstracts, plenary lectures, oral and poster sessions, p. 100.
- Della Vedova, B., Pellis, G., Lawver, L.A. & Brancolini, G., 1992. Heat flow and tectonics of the Western Ross Sea, in *Recent Progress in Antarctic Earth Science*, pp. 627–637, eds Yoshida, Y., Kaminuma, K. & Kazuyuki, S., Terrapub, Tokyo.
- Della Vedova, B., Pellis, G., Trey, H., Zhang, J., Cooper, A.K., Makris, J. & the ACRUP working group, 1997. Crustal structure of the Transantarctic Mountains, Western Ross Sea, in *The Antarctic Region: Geological Evolution and Processes*, pp. 609–618, ed. Ricci C.A., Terra Antarctica Publication, Siena.
- Fitzgerald, P.G., 1992. The Transantarctic Mountains of southern Victoria Land: The application of apatite fission track analysis to a rift shoulder uplift, *Tectonics*, **11**, 634–662.
- Fitzgerald, P.G., 1995. Cretaceous and Cenozoic exhumation of the Transantarctic Mountains: evidence from the Kukri Hills of southern Victoria Land compared to fission track data from gneiss at DSDP site 270, in *The Antarctic Region: Geological Evolution and Processes*, p. 133, ed. Ricci C.A., Terra Antarctica Publication, Siena.
- Fitzgerald, P.G., Sandiford, T., Barrett, P.J. & Gleadow, A.W., 1986. Asymmetric extension associated with uplift and subsidence in the Transantarctic Mountains and Ross Embayment, *Earth planet. Sci. Lett.*, **81**, 67–78.
- Goldstein, P., Dodge, D. & Firpo, M., 1999. SAC2000: Signal processing and analysis tools for seismologists and engineers. UCRL-JC-135963, *Invited contribution to the IASPEI International Handbook of Earthquake and Engineering Seismology*.
- Hamilton, R.J., Luyendyk, B.P., Sorlien, C.C. & Bartek, L.R., 2001. Cenozoic tectonics of the Cape Roberts Rift Basin and Transantarctic Mountains Front, Southwestern Ross Sea, Antarctica, *Tectonics*, **20**, 325–342.
- Heiskanen, W.A. & Vening Meinesz, F.A., 1958. *The Earth and its Gravity Field*, McGraw-Hill, New York, p. 470.
- Isaac, M.J., Chinn, T.J., Edbrooke, S.W. & Forsyth, P.J., 1995. Geology of the Olympus Range area, southern Victoria Land, Antarctica, scale 1:50 000, *Institute of Geological & Nuclear Sciences geological map 20*, 1 sheet + 60 p. IGNS, Lower Hutt, New Zealand.
- Langston, C.A., 1977. The effect of planar dipping structure on source and receiver responses for constant ray parameter, *Bull. seism. Soc. Am.*, **67**, 1029–1050.
- LeMasurier, W., 1990. Late cenozoic volcanism on the antarctic plate—an overview, in *Volcanoes of the Antarctic Plate and Southern Oceans AGU Antarc. Res. Ser.*, Vol. 48, pp. 1–17, eds LeMasurier, W. & Thompson, J.W.
- Levin, V. & Park, J., 1997. Crustal anisotropy in the Ural Mountains foredeep from teleseismic receiver functions, *Geophys. J. Int.*, **24**, 283–1286.
- Ligorria, J.P. & Ammon, C.J., 1999. Iterative deconvolution and receiver-function estimation, *Bull. seism. Soc. Am.*, **89**, 1395–1400.
- McGinnis, L.D., Bowen, R.H., Erickson, J.M., Allred, B.J., Kremer, J.L., 1985. East-West Antarctic boundary in McMurdo Sound, *Tectonophysics*, **114**, 341–356.
- O'Connell, D.R.H. & Stepp, T.M., 1993. Structure and Evolution of the crust at the Transantarctic Mountains—Ross Sea crustal transition: Results from the Tourmaline plateau seismic array of the GANOVEX V Ship-to-shore seismic refraction experiment, *Geol. Jb.*, **47**, 229–276. Hannover.
- Owens, T.J. & Zandt, G., 1985. The response of the continental crust-mantle boundary observed on broadband teleseismic receiver functions, *Geophys. Res. Lett.*, **12**, 705–708.
- Owens, T.J., Crosson, R.S. & Hendrickson, M.A., 1988. Constraints on the subduction geometry beneath western Washington from broadband teleseismic waveform modeling, *Bull. seism. Soc. Am.*, **78**, 1319–1334.
- Park, J. & Levin, V., 2000. Receiver functions from multiple-taper spectral correlation estimates, *Bull. seism. Soc. Am.*, **90**, 1507–1520.
- Peng, X. & Humphreys, E.D., 1997. Moho dip and crustal anisotropy in northwestern Nevada from teleseismic receiver functions, *Bull. seism. Soc. Am.*, **87**, 745–754.

- Pondrelli, S., Amoto, A., Chiappini, M., Cimini, G.B., Colmo, D. & Di Bona, M., 1997. ACRUP1 Geotraverse: Contribution of teleseismic data recorded on land, in *The Antarctic Region: Geological Evolution and Processes*, pp. 631–635, ed. Ricci, C.A., Terra Antarctica Publication, Siena.
- Pyne, A., 1984. Geology of the Mt Fleming area, South Victoria Land, Antarctica, *New Zealand journal of geology and geophysics*, **27**, 505–512.
- Redfield, T.F. & Behrendt, J.C., 1992. Gravity modeling across the Transantarctic Mountains, Northern Victoria Land, in *Recent Progress in Antarctic Earth Science*, pp. 535–544, eds Yoshida, Y., Kaminuma, K. & Kazuyuki, S., Terrapub, Tokyo.
- Reitmayr, G., 1997. Gravity studies of Victoria Land and the adjacent oceans, Antarctica, in *The Antarctic Region: Geological Evolution and Processes*, pp. 597–602, ed. Ricci, C.A., Terra Antarctica Publication, Siena.
- Sambridge, M., 1998. Exploring multidimensional landscapes without a map, *Inverse problems*, **14**, 427–440.
- Sambridge, M., 1999a. Geophysical inversion with a neighbourhood algorithm—I. Searching a parameter space, *Geophys. J. Int.*, **138**, 479–494.
- Sambridge, M., 1999b. Geophysical inversion with a neighbourhood algorithm—II. Appraising the ensemble, *Geophys. J. Int.*, **138**, 727–746.
- Savage, M.K., 1998. Lower crustal anisotropy or dipping boundaries? Effect on receiver functions and a case study in New Zealand, *J. geophys. Res.*, **103**, 15 069–15 087.
- Sheehan, A.F., Abers, G.A., Jones, C.H. & Lerner-Lam, A.L., 1995. Crustal thickness variations across the Colorado Rocky Mountains from teleseismic receiver functions, *J. geophys. Res.*, **100**, 20 391–20 404.
- Shibutani, T., Sambridge, M. & Kennett, B.L.N., 1996. Genetic algorithm inversion for receiver functions with application to crust and uppermost mantle structure beneath Eastern Australia, *Geophys. Res. Lett.*, **23**, 1829–1832.
- Smithson, S.B., 1972. Gravity interpretations in the Trans-Antarctic Mountains near McMurdo Sound, Antarctica, *Geol. Soc. Am. Bull.*, **83**, 3437–3442.
- Stern, T.A. & ten Brink, U.S., 1989. Flexural uplift of the Transantarctic Mountains, *J. geophys. Res.*, **94**, 10 315–10 330.
- Stern, T.A., ten Brink, U.S. & Bott, M.H.P., 1992. Numerical modelling of uplift and subsidence adjacent to the Transantarctic Mountain Front, in *Recent Progress in Antarctic Earth Science*, 627–637, eds Yoshida, Y., Kaminuma, K. & Kazuyuki, S., Terrapub, Tokyo.
- Sugden, D.E., Summerfield, M., Denton, G., Wilch, T., McIntosh, W., Marchant, D. & Rutford, R., 1999. Landscape development in the Royal Society Range, southern Victoria Land, Antarctica: stability since the Miocene, *Geomorphology*, **28**, 181–200.
- ten Brink, U.T. & Stern, T., 1992. Rift flank uplifts and hinterland basins: Comparison of the Transantarctic Mountains with the great escarpment of southern Africa, *J. geophys. Res.*, **97**, 569–585.
- ten Brink, U.T., Bannister, S., Beaudoin, B.C. & Stern, T.A., 1993. Geophysical Investigations of the tectonic boundary between East and West Antarctica, *Science*, **261**, 45–50.
- ten Brink, U.T., Hackney, R.I., Bannister, S., Stern, T.A. & Makovsky, Y., 1997. Uplift of the Transantarctic Mountains and the bedrock beneath the East Antarctic ice sheet, *J. geophys. Res.*, **102**, 27 603–27 621.
- Trehu, A.M., Holt, T., Behrendt, J.C. & Fritsch, J.C., 1989. Crustal structure in the Ross Sea, Antarctica: preliminary results from GANOVEX V (abstract), *EOS, Trans. Am. geophys. Un.*, **70**, 1344.
- Trey, H., Makris, J., Brancolini, G., Cooper, A.K., Cochrane, G., Della Vedova, B. & ACRUP Working Group, 1997. The Eastern Basin crustal model from wide-angle reflection data, Ross Sea, Antarctica, in *The Antarctic Region: Geological Evolution and Processes*, pp. 643–648, ed. Ricci, C.A., Terra Antarctica Publications, Siena.
- Turnbull, I.M., Allibone, A.H., Forsyth, P.J. & Heron, D.W., 1994. Geology of the Bull Pass-St Johns Range area, Southern Victoria Land, Antarctica, scale 1:50 000, *Institute of Geological & Nuclear Sciences geological map 14*, 1 sheet + 52 p., IGNS, Lower Hutt, New Zealand.
- Veevers, J.J. & Eittreim, S.L., 1988. Reconstruction of Antarctica and Australia at breakup ( $95 \pm 5$  Ma) and before rifting (160 Ma), *Aust. J. earth. Sciences*, **35**, 355–362.
- Wiens, D.A., Anandakrishnan, S., Nyblade, A., Fisher, J.J., Pozgay, S., Shore, P.J. & Voigt, D., 2003. Preliminary results from the Trans-Antarctic Mountains Seismic Experiment, in *9th International Symposium on Antarctic Earth Sciences, Programme and Abstracts*, p. 340, ed. Fütlerer, D.K., Alfred-Wegener-Stiftung, Berlin.